RSC Advances

ROYAL SOCIETY OF CHEMISTRY

www.rsc.org/advances

Table of contents entry

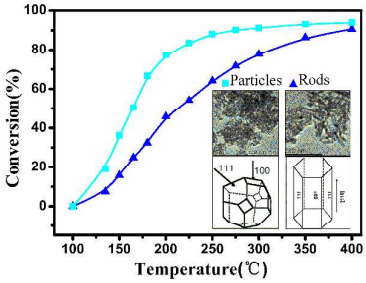

Morphology engineering of CeO_2 improves catalytic performance and catalytic materials that have increased activity can be obtained through morphology-controlled synthesis.

Journal Name

RSCPublishing

ARTICLE

Effect of Ceria morphology on the activity of MnO_x/CeO_2 catalysts for the catalytic combustion of chlorobenzene

Cite this: DOI: 10.1039/x0xx00000x

Pei Zhao, Chengnan Wang, Fei He and Shangtang Liu*

Received 00th January 2012,
Accepted 00th January 2012

DOI: 10.1039/x0xx00000x

www.rsc.org/

The effect of CeO_2 morphology on the performance of a MnO_x/CeO_2 catalyst was investigated for the catalytic combustion of chlorobenzene (CB), which was used as a model compound for chlorinated volatile organic compounds (CVOCs). The catalytic activity tests revealed that MnO_x/CeO_2 nanoparticles (NPS) achieved relatively higher CB conversions than MnO_x/CeO_2 nanorods (NR). The MnO_x/CeO_2 catalysts were characterized by X-ray diffraction (XRD), Raman spectroscopy, Brunauer-Emmett-Teller (BET) N_2 adsorption, transmission electron microscopy (TEM), X-ray photoelectron spectroscopy (XPS) and hydrogen temperature-programmed reduction (H_2-TPR). The characterization of the MnO_x/CeO_2 catalysts indicated that CeO_2-NPS had a higher exposure of the (100) crystal plane and possessed more Mn^{4+} species, oxygen vacancies and surface-adsorbed oxygen. It was suggested that the CeO_2-NPS had a stronger interaction with MnO_x species, which resulted in greater catalytic activity in the combustion of CB. The catalytic activity of MnO_x/CeO_2-NPS could be attributed to higher concentrations of Mn^{4+} species, oxygen vacancies, and surface-adsorbed oxygen, which were associated with the exposed (100) crystal planes. Therefore, these results demonstrated that the catalytic performance of MnO_x/CeO_2 catalyst was greatly affected by CeO_2 morphology. Therefore, catalytic materials that have increased activity can be obtained through morphology-controlled synthesis.

1. Introduction

Chlorinated volatile organic compounds (CVOCs) which are mainly generated from industrial processes, and medical wastes are recognized as major contributors to air pollutants.[1,2] Generally, CVOCs can lead to photochemical smog and are highly toxic to humans and animals.Therefore, it is essential to develop practical and cost-effective methods to eliminate CVOCs in gases. Of the available techniques, catalytic combustion is one of the most effective technologies for the removal of destruction of CVOCs emissions due to its high removal efficiency and low operating temperature.

Among the catalysts used for the catalytic combustion of CVOCs, manganese oxides are known to be active catalysts on account of their high oxygen storage ability and redox properties.[3-8] Furthermore, catalysts based on MnO_x supported on metal oxides, such as MnO_x/CeO_2 and MnO_x/TiO_2 catalysts, have been reported to display higher catalytic performance for the oxidation of CVOCs compared with MnO_x catalysts alone.[9-11] Accordingly, the nature of the support material is critical to the catalytic performance of MnO_x-based catalysts.[12-15] In particular, the support material ceria has been widely utilized for the MnO_x-based catalyzed oxidation of chlorobenzene (CB) due to its high oxygen storage capacity (OSC) and reducibility in the oxidation of CVOCs. Reports have shown that the capacity for oxygen storage is dependent on the morphology of ceria.[10,16,17] Thus far, several studies document the shape effects of ceria in CO oxidation, ethanol steam reforming, and NO reduction with NH_3. Huang and co-workers[18] investigated the catalytic performance of various Au-supported ceria shapes for CO oxidation. They found that predominantly exposed (100)/(110) surface structures of ceria nanorods are superior for dispersing and stabilizing Au nanoclusters. This leads to a higher redox activity for CO oxidation, while relatively reducing the dispersal of Au nanoclusters on the exposed (111) plane for ceria nanoparticles, as determined by its lower activity

for CO oxidation. Soykal and co-workers[16] also indicated that CeO_2 nanocubes were more active for ethanol steam reforming than ceria nanorods due to the presence of a higher exposure of the (110) plane for nanocubes.

Additional studies revealed that MnO_x/CeO_2 catalysts exhibited excellent catalytic performance in the combustion of CB. However, to the best our knowledge, little attention has been given to the morphology dependence of ceria nanomaterials in Mn species deposited on CeO_2 for the catalytic combustion of CB. Additionally, various ceria morphology supports may possess different capacities for oxygen storage,[19] which can then influence the catalytic performance of Mn species. Herein, we present the effect of ceria morphology on a Mn-based catalytic system for the catalytic combustion of CB. Ceria nanorods and ceria nanoparticles were synthesized by hydrothermal and co-precipitation methods, respectively. A wet impregnation method was utilized to incorporate manganese oxides over CeO_2 nanomaterials. The catalytic performance of MnO_x/CeO_2 nanomaterials with two different shapes was examined in the catalytic combustion of CB.

2. Experimental Section

2.1 Preparation

CeO_2 nanorods were prepared by the hydrothermal method as follows.[20] $Ce(NO_3)_3{\cdot}6H_2O$ (3.45 mmol) was dissolved in deionized water (5 mL) and mixed with an aqueous sodium hydroxide aqueous solution (C_{NaOH} = 6 M). The mixture was then stirred at room temperature for 30 min to obtain a milky slurry and subsequently transferred to a 50 mL autoclave, sealed, and heated at 100 °C for 24 h. After the hydrothermal treatment, the resulting precipitate was filtered, washed thoroughly with deionized water, and dried at 60 °C, and finally, calcination occurred at 400°C for 4 h. The CeO_2 nanoparticles were prepared by the precipitation method that has been reported in the literature.[21] $Ce(NO_3)_3{\cdot}6H_2O$ was dissolved in distilled water, and the pH value of the solution was rapidly adjusted to pH 12 with a 10 % NaOH solution with stirring. The precipitate was filtered, washed with deionized water, and dried at 60 °C for 12 h, and then, calcination occurred at 400 °C for 4 h. The synthesized CeO_2 nanorods and CeO_2 nanoparticles were denoted as CeO_2-NR and CeO_2-NPS, respectively.

MnO_x/CeO_2 catalysts with different morphologies were prepared by incipient wetness impregnation. Manganese was loaded onto the CeO_2 support with 50 % $Mn(NO_3)_2$. The manganese loading was selected as 11 wt % (Mn/(Ce+Mn)=0.27, molar ratio). Following impregnation, the catalysts were aged at room temperature for 24 h and dried at 80 °C in air overnight, and calcination took place at 400 °C for 4 h. The MnO_x/CeO_2 nanorods and MnO_x/CeO_2 nanoparticles were denoted as MnO_x/CeO_2-NR and MnO_x/CeO_2-NPS, respectively.

2.2 Characterization techniques

Transmission electron microscopy (TEM) tests were recorded on a JEM-2100 electron microscope operating at 200 kV.The samples were ultrasonically dispersed in ethanol and deposited on copper grids coated with lacey carbon. Energy dispersion spectra (EDS) were performed on a FALCON 80 X-ray energy-dispersive spectrometer that was used for the elemental analysis of the samples. X-ray diffraction (XRD) patterns of the MnO_x/CeO_2 and bare CeO_2 were collected on a Bruker D8 Advance X-ray diffractometer using Cu Kα radiation (λ=1.5405 Å) operated at 40 kV and 50 mA. The diffraction patterns were taken in the 2θ angle of 20-70º. The BET surface areas of the catalysts were obtained from N_2 adsorption and desorption tests at 77 K using a NOVA2000e analyzer. The samples were degassed at 120 °C for 12 h before measurements were taken. The Raman spectra were recorded on a laser confocal miscroscopy Raman spectrometer (DXR, American Thermo Electron) operated at a wavelength of 532 nm. XPS measurements were carried out with a VG Multilab 2000 spectrometer using Al Kα (hν = 1253.6 eV) radiation. The TPR runs were conducted with a linear heating rate (10 °C/min) in a flow of 10% H_2 in argon at a flow rate of 40 mL/min. Hydrogen consumption was measured quantitatively by a thermal conductivity detector (TCD), which was calibrated by quantitative reduction of a given quantity of CuO to metallic copper.

2.3 Catalytic activity tests

Catalytic activity tests were performed in a fixed-bed flow reactor made of an 8 mm inner diameter quartz tube under an atmospheric pressure between 100–400 °C. Two-hundred milligrams of the (50-80 mesh) catalysts were placed in the reactor. The feed gas consisted of 5000 ppm CB, 20% O_2, and balanced N_2. The total flow rate was 100 mL/min, with the gas hourly space velocity (GHSV) at 20,000 h^{-1}. The effluent was analyzed by an on-line gas chromatograph (GC) equipped with a flame ionization detector (FID) for the quantitative analysis of CB.

3. Results and discussion

3.1 XRD and N_2 adsorption results

The BET surface areas of the supports and MnO_x/CeO_2 nanostructures are listed in Table 1. The BET surface area of CeO_2-NR and CeO_2-NPS were 113.4 and 127.7 $m^2\ g^{-1}$, respectively. After loading MnO_x, the specific surface areas of the MnO_x/CeO_2-NR and MnO_x/CeO_2-NPS decreased to 79.5 and 82.4 $m^2\ g^{-1}$. Compared with the BET surface area of CeO_2-NR and CeO_2-NPS, a decrease in the specific surface areas of MnO_x/CeO_2-NR and MnO_x/CeO_2-NPS can be attributed to pore blockage by MnO_x.[22]

X-ray diffraction patterns of MnO_x/CeO_2 nanostructures with different morphologies are shown in Fig. 1. All of the diffraction peaks were attributed to the cubic phase of CeO_2 (JCPDS 34-0394), but no peaks of manganese oxides were observed, indicating a high dispersion of MnO_x on the CeO_2 nanostructures. Moreover, diffraction peaks of MnO_x/CeO_2-NR were broader compared with those of MnO_x/CeO_2-NPS, suggesting the formation of a smaller size of MnO_x/CeO_2 -NPS. CeO_2 crystallite sizes were calculated by the Scherrer equation, and the results (Table 1) indicated that CeO_2-NR and CeO_2-NPS were 15.1 and 9.8 nm, respectively, which are in agreement with the TEM results. Table 2 shows the peak intensities normalized with respect to the peak intensity of the (111) plane of ceria for the MnO_x/CeO_2-NPS and MnO_x/CeO_2-NR. As shown in Table 2, the (220) plane for both catalysts possessed similar relative intensities, while the (200) plane showed significantly higher diffraction for MnO_x/CeO_2-NPS, with a 45% relative intensity compared to 30% for MnO_x/CeO_2-NR. This indicates that the CeO_2-NPS morphology may expose more of the (100) plane compared with CeO_2-NR.

Table 1 The properties of the different catalysts

sample	Surface area (m^2/g)	D(CeO_2) (nm)/ by XRD[a]	D(CeO_2) (nm)/by TEM
CeO_2-NR	113.4	—	—
CeO_2-NPS	127.7	—	—
MnO_x/CeO_2-NR	79.5	15.1	13–90
MnO_x/CeO_2-NPS	82.4	9.8	10±2

[a] From the Scherrer equation, based on the (111) reflection of the CeO_2.

Table 2 XRD intensities for MnO_x/CeO_2 catalysts normalize with respect to CeO_2 (111) reflection

2θ	28.5	33.0	47.5	56.3
Respective Planes	CeO_2 (111)	CeO_2 (200)	CeO_2 (220)	CeO_2 (311)
MnO_x/CeO_2-NR	100%	30%	56%	40%
MnO_x/CeO_2-NPS	100%	45%	57%	45%

Si and co-workers reported that the formation energies for oxygen vacancies for ceria oxide surface follow the sequence (111) > (100).[23] Therefore, the (100) plane more readily form oxygen vacancies. It is also conceivable that the introduction of oxygen vacancies assists in improving catalyst performance significantly.[16] Therefore, more (100) plane on the MnO_x/CeO_2-NPS may help improve the catalytic performance.

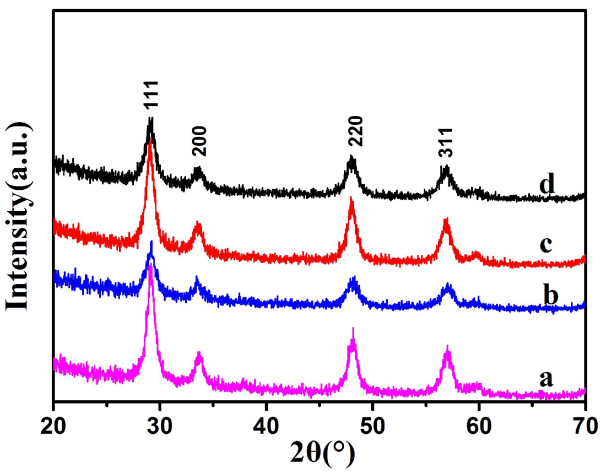

Fig. 1 XRD patterns of (a) CeO_2-NR, (b) CeO_2-NPS, (c) MnO_x/CeO_2-NR, and (d) MnO_x/CeO_2-NPS.

3.2 TEM and HRTEM results

The TEM images, structural models, and EDS spectra of synthesized materials are shown in Fig. 2. The two different CeO_2 nanomaterials maintain their original crystal shapes after deposition of MnO_x. MnO_x/CeO_2-NR has a uniform diameter of 10 ± 3 nm and a length within 13–90 nm. Fig. 2b shows the HRTEM image of MnO_x/CeO_2-NR. It can be observed that MnO_x/CeO_2-NR exposed the (100) and (111) planes, with an interplanar spacing of 0.27 nm and 0.31 nm, respectively. The structural model of the MnO_x/CeO_2-NR is shown in Fig. 2c. The single crystal nanorod grew along the [110] direction. Fig. 2c shows the MnO_x/CeO_2-NR hexangular prism enclosed by four (111) and two (100) planes.[20] The TEM image of MnO_x/CeO_2-NPS (Fig. 2e) reveals that the nanoparticles have a size of 10 ± 2 nm. The structural model of the MnO_x/CeO_2-NPS shows that MnO_x/CeO_2-NPS is approximately determined to be the truncated octahedra which was surrounded by eight (111) and six (100) planes.[24] The EDS spectra in Fig. 2d, h shows that the actual content of Mn element for MnO_x/CeO_2-NR and MnO_x/CeO_2-NPS were 11.39 wt % and 16.50 wt %, respectively. In addition, the EDS spectra in Fig. 2d, h confirms the presence of Mn and suggests that the MnO_x species are highly dispersed on the surface of the CeO_2 nanostructure.

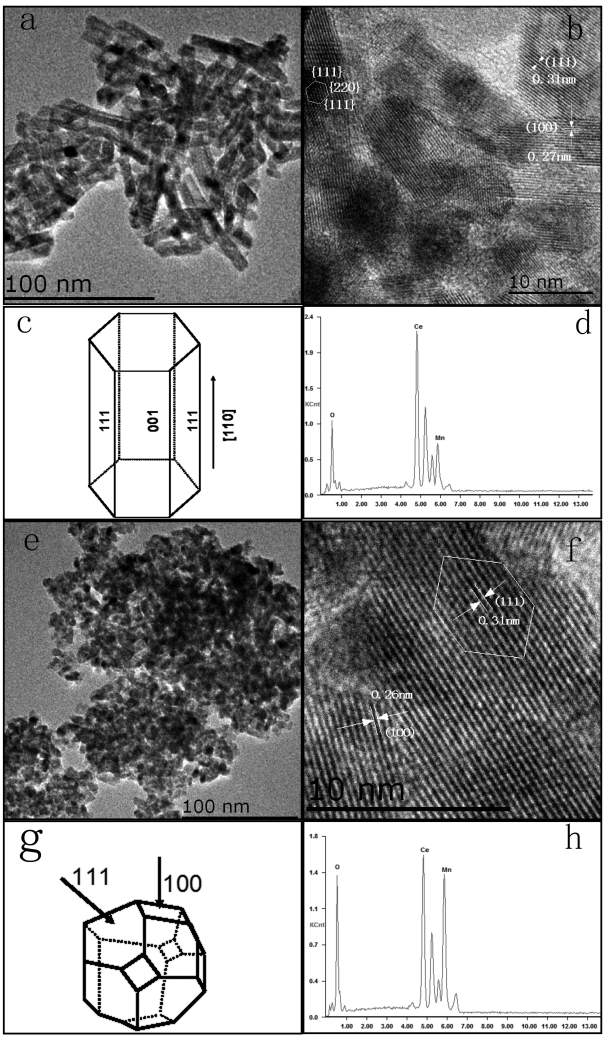

Fig. 2 TEM and HRTEM images of (a, b) MnO_x/CeO_2-NR, (e, f) MnO_x/CeO_2-NPS; the structural model of (c) MnO_x/CeO_2-NR, (g) MnO_x/CeO_2-NPS; EDS patterns of (d) MnO_x/CeO_2-NR, (h) MnO_x/CeO_2-NPS.

3.3 H_2 -TPR results

Fig. 3 displays the H_2-TPR profiles of the CeO_2 and MnO_x/CeO_2 nanostructures. For CeO_2-NR, the reduction of CeO_2 starts at 350 °C and a broad peak centered at 490 °C, which is attributed to the reduction of the surface oxygen of CeO_2.[25] Meanwhile, CeO_2-NPS shows a similar reduction profile at a slightly higher temperature (540°C), while the MnO_x/CeO_2 nanostructures showed different profiles of the reduction peaks. MnO_x/CeO_2-NR showed three distinct reduction peaks, with a shoulder peak at 368 °C. The peak at 227 °C could be attributed to reduction of MnO_2 to Mn_2O_3, and the peak at 302 °C, with a shoulder peak at 368 °C, was a further reduction of Mn_2O_3 to Mn_3O_4, while the peak at 475 °C ascribed to the combined reductions of Mn_3O_4 to MnO and surface oxygen removal of ceria.[24,26-30] A similar reduction profile was observed for MnO_x/CeO_2-NPS, except that the reduction peaks shifted to higher temperature regions, indicating that interaction between MnO_x and CeO_2-NPS is stronger than that with CeO_2-NR. Quantitative evaluation of the reduction peaks (Table 3) revealed that the H_2 consumption of the first two peaks on the MnO_x/CeO_2-NPS is greater than the MnO_x/CeO_2-NR, demonstrating that MnO_x/CeO_2-NPS has more surface oxygen and that a larger quantity of strongly interactive MnO_x species exist on the CeO_2-NPS.[26] Therefore, the more surface oxygen on CeO_2-NPS and the stronger interaction between MnO_x and CeO_2-NPs in the higher oxidative ability of the MnO_x species.[31]

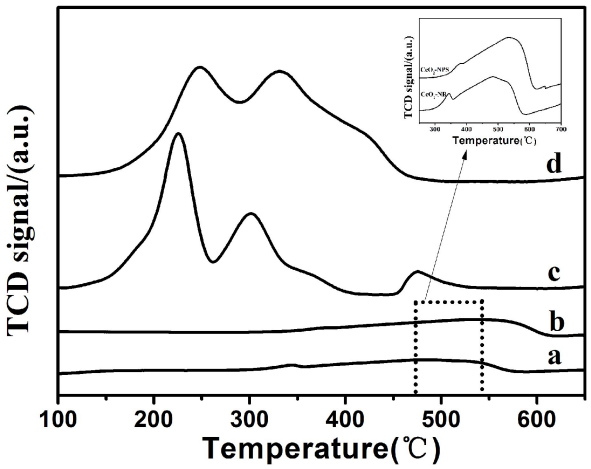

Fig. 3 H_2-TPR profiles of (a) CeO_2-NR, (b) CeO_2-NPS, (c) MnO_x/CeO_2-NR, and (d) MnO_x/CeO_2-NPS

Table 3 Hydrogen consumption of H_2-TPR tests

Sample	T(°C)	mmol g^{-1}	T(°C)	mmol g^{-1}
MnO_x/CeO_2-NR	227	0.77	302	0.89
MnO_x/CeO_2-NPS	245	0.86	331	1.14

3.4 Raman spectra

The Raman spectra of CeO_2 and MnO_x/CeO_2 nanostructures are presented in Fig. 4. A distinct F_{2g} symmetry mode of the CeO_2 phase at approximately 462 cm^{-1} can be observed in the Raman spectra of the CeO_2 nanostructures (Fig. 4a).[32] Furthermore, two additional weak peaks, at approximately 600 and 1180 cm^{-1}, can also be observed in the Raman spectra of CeO_2 nanomaterials (Fig. 4a). These are attributed to the defect-induced (D) mode and the second-order longitudinal (2LO) mode, respectively.[28] A similar Raman spectrum was observed for MnO_x/CeO_2 nanostructures (Fig. 4b), except that the peak at 600 cm^{-1} for oxygen vacancies displayed a blue shift to 650 cm^{-1}, and the peak at 1180 cm^{-1} shifted to 1170 cm^{-1}. These shifts can be attributed to the Mn incorporation in the CeO_2 lattice. Additionally, the new peak at 577cm^{-1} can be assigned to the Mn-Ce-O bond on the MnO_x/CeO_2 nanostructures.

The Raman peak at 600 cm^{-1} was related to the oxygen vacancies induced by the presence of Ce^{3+} ions, and the I_{600}/I_{462} value (Fig. 4c) reflects the degree of the defect sites on nanostructures, such as the relative content of the oxygen vacancies.[32,33] From Fig. 4c, the intensity ratio I_{600}/I_{462} follows the sequence: MnO_x/CeO_2-NPS > MnO_x/CeO_2-NR > CeO_2-NPS > CeO_2-NR, indicating that MnO_x/CeO_2-NPS possessed

the greatest amount of oxygen vacancies. According to Fig. 4c, the I_{600}/I_{462} value increased dramatically when manganese ions were doped into the ceria lattice. This indicated that Mn ions incorporated into the CeO_2 phase and thus led to an increase in the degree of defects. Clearly, MnO_x/CeO_2-NPS exhibited the higher value of I_{600}/I_{462} compared to the MnO_x/CeO_2-NR nanostructure, demonstrating that the interaction between MnO_x and CeO_2-NPS is stronger than with CeO_2-NR. In summary, the Raman results reflect that the stronger interaction between MnO_x and CeO_2-NPS, and in turn, MnO_x/CeO_2-NPS incorporated into a greater oxygen vacancies, which is in accordance with the H_2-TPR result.

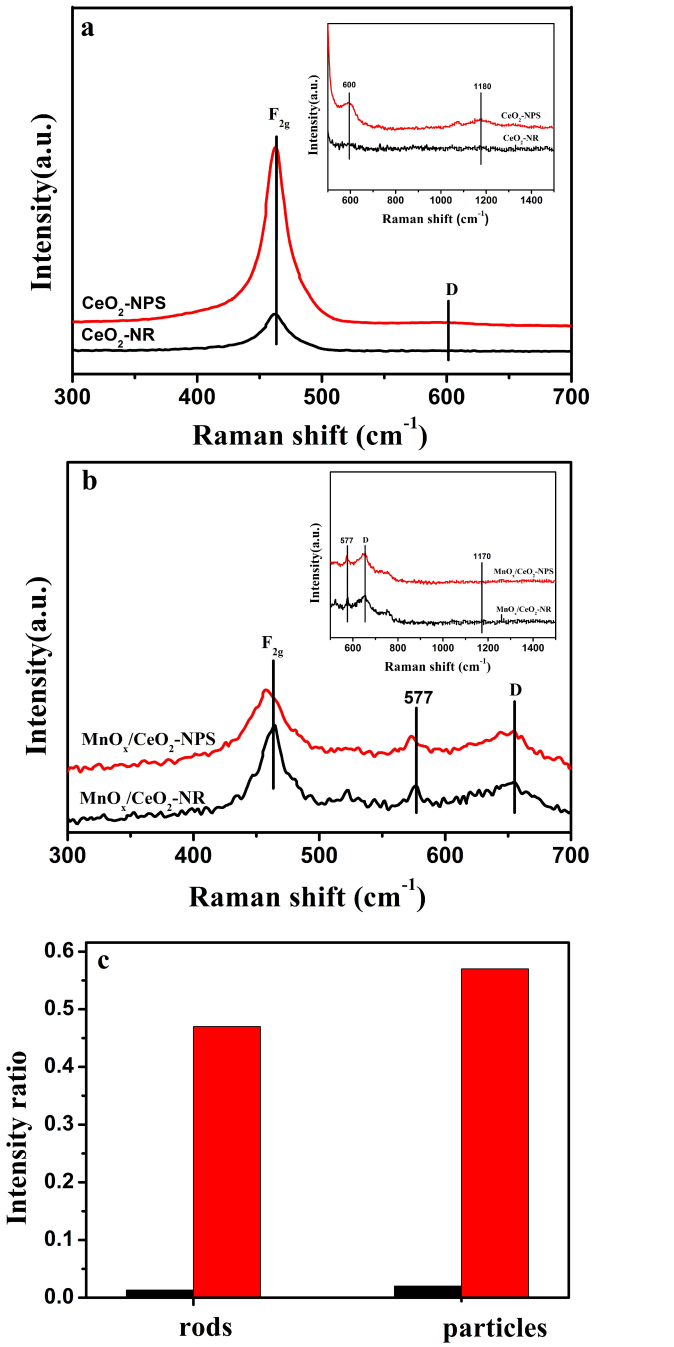

Fig. 4 Raman spectra of (a) CeO_2, (b) MnO_x/CeO_2 nanostructures, and (c) the peak intensity ratios of I_{600}/I_{400} over CeO_2 (black column) and MnO_x/CeO_2 nanostructures (red column).

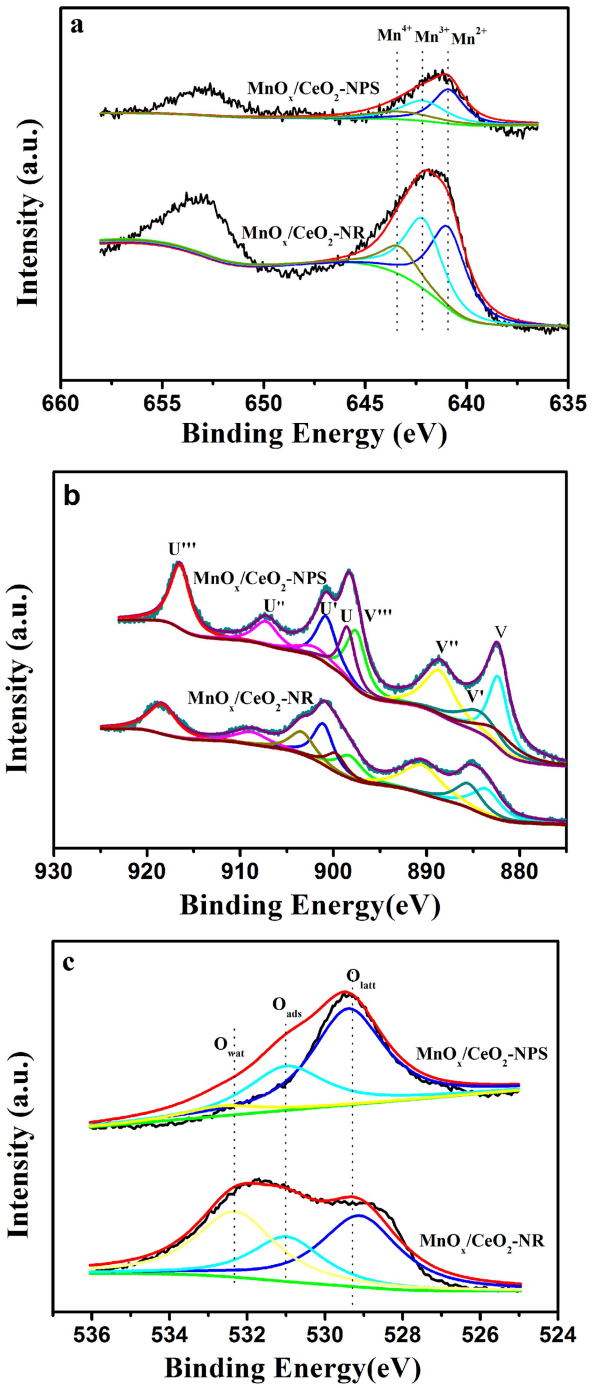

Fig. 5 (a) Mn2p, (b) Ce 3d and (c) O 1S XPS spectra of MnO_x/CeO_2 nanostructures.

3.5 XPS results

The Mn 2p, O 1s, and Ce 3d XPS spectra of the MnO_x/CeO_2-NR and MnO_x/CeO_2-NPS catalysts are shown in Fig. 5. As shown in Fig. 5a, the Mn $2P_{3/2}$ spectra can be separated into three peaks. The binding energy at ca. 640.5, 641.8, and 643.7

Table 4 Surface Chemical and States Based on XPS Analysis

sample	Mn^{4+} (%)[a1]	Mn^{3+} (%)[a2]	Mn^{2+} (%)[a3]	Ce^{3+} (%)	O_{latt} (%)	O_{ads} (%)	O_{wat} (%)
MnO_x/CeO_2-NR	15.6	38.8	45.5	26.4	40.0	23.0	36.9
MnO_x/CeO_2-NPS	21.1	37.0	41.9	29.0	58.0	31.0	6.9

a1+a2+a3=100%

eV corresponded to Mn^{2+}, Mn^{3+}, and Mn^{4+},[34] respectively. The concentration of Mn^{4+} on MnO_x/CeO_2-NPS is higher than on MnO_x/CeO_2-NR, as shown in Table 4. Liao and co-workers [26] reported that high Mn^{4+} could lead to oxygen vacant sites on catalysts. Accordingly, a higher ratio of Mn^{4+} on the CeO_2-NPS may lead to more oxygen vacancies.

The Ce 3d spectra of the MnO_x/CeO_2-NR and MnO_x/CeO_2-NPS are shown in Fig. 5b. The peaks at approximately U, U'', U''', V, V'', and V''' are attributed to Ce^{4+}, and the Ce^{3+} can be fitted with the peaks at U' and V'. The concentrations of Ce^{3+} on the MnO_x/CeO_2-NR and MnO_x/CeO_2-NPS are 26.4 %, and 29.0 %, respectively. Liu and co-workers[35] suggested that a higher Ce^{3+} concentration can produce more oxygen vacancies on catalysts. The spectra indicates that MnO_x/CeO_2-NPS contain more oxygen vacancies than MnO_x/CeO_2-NR.

The O 1s spectra of MnO_x/CeO_2-NR and MnO_x/CeO_2-NPS are shown in Fig. 5c. The O 1s profile can be fit into three peaks: lattice oxygen (O_{latt}) at 529.4-530.0 eV, surface-adsorbed oxygen (O_{ads}) at 531.0-531.7 eV and adsorbed molecular water (O_{wat}) at approximately 532.7 eV.[36] Quantitatively, it can be observed in Table 4 that the O_{ads}/O_{wat} +O_{ads} +O_{latt} ratio of MnO_x/CeO_2-NPS catalyst is higher than MnO_x/CeO_2-NR, indicating that MnO_x/CeO_2-NPS catalyst are rich in surface-adsorbed oxygen. Because O_{ads} is more active than O_{latt} due to its high mobility, the higher concentration of O_{ads} is helpful for the CB oxidation.[37]

3.6 Characteristic of the used catalysts

The morphologies of the used MnO_x/CeO_2-NR and MnO_x/CeO_2-NPS catalysts were observed on TEM images in Fig. 6. The used MnO_x/CeO_2-NR has a uniform diameter of 11 ± 3 nm and a length within 13–95 nm while the MnO_x/CeO_2-NPS have a size of 9 ± 2 nm. This indicates that the grain size of the used catalysts basically remains unchanged after reaction. The catalysts still maintain their shapes after reaction, indicating that the MnO_x/CeO_2 nanostructures have structure stability during CB combustion.

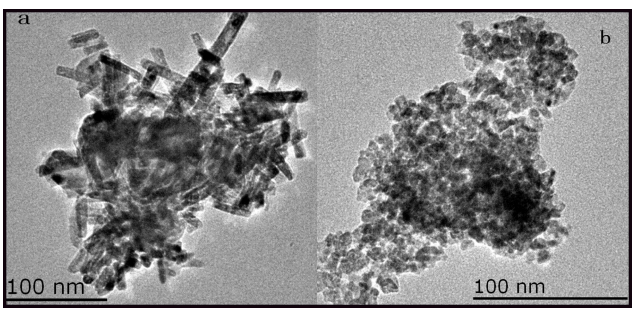

Fig. 6 TEM images of the used catalysts: (a) MnO_x/CeO_2-NR, (b) MnO_x/CeO_2-NPS.

The XRD patterns of the used MnO_x/CeO_2 nanostructures are shown in Fig. 7. All typical diffraction peaks can be attributed to the ceria fluorite structure (JCPDS 34-0394), and no peaks of MnO_x were observed. This phenomenon demonstrates that a strong interaction between the MnO_x and CeO_2 nanostructures exists, which prevents the agglomeration of MnO_x during CB combustion .[28]

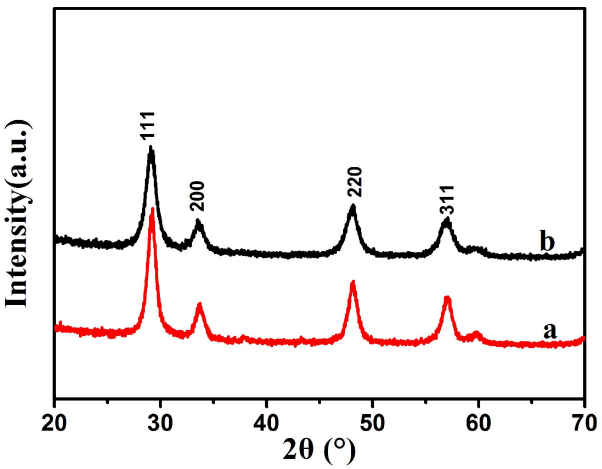

Fig. 7 XRD patterns of the used catalysts: (a) MnO_x/CeO_2-NR , (b)MnO_x/CeO_2-NPS.

3.7 Catalytic activity and stability of catalysts

The catalytic performance of the bare CeO_2 supports and MnO_x/CeO_2 catalysts for the catalytic combustion of CB is shown in Fig. 8. As shown in Fig. 8, both CeO_2-NPS and CeO_2-NR supports exhibit poor activity for catalytic combustion of CB, although the CeO_2-NPS is slightly more active. After loading Mn, the activities of the Mn-supported catalysts were markedly enhanced, revealing the necessity for Mn in the catalytic combustion of CB. Additionally, a significant effect of support morphology on catalyst performance can be observed in Fig. 8. The MnO_x/CeO_2-NPS catalyst displayed higher activity than MnO_x/CeO_2-NR. At 275 °C, the CB conversions was 90.0 % over MnO_x/CeO_2-NPS, while only 71.7 % over MnO_x/CeO_2-NR. This indicates that MnO_x/CeO_2-NPS catalysts showed a better catalytic activity than the MnO_x-CeO_2 mixed oxides (90% conversion at 300 °C, Mn/(Mn+Ce)=0.27, molar ratio) reported by wang et al.[1]

Because the obtained MnO_x/CeO_2 catalysts have different exposed planes, this may be one possible explanation for the observed difference in catalytic performance of the two catalysts. Because CeO_2-NPS support preferentially exposes the (100) plane and this plane is more likely to create anion vacancies and defects, it is reasonable that this support offers more oxygen vacancies.[16] As detected by the Raman and XPS

results, the MnO_x/CeO_2–NPS sample has more oxygen vacancies. Previous reports on this subject have described that the introduction of oxygen vacancies on support material were conducive to adsorbing oxygen and forming highly reactive atomic oxygen, which would significantly improve the catalyst performance.[21,38]Therefore, additional oxygen vacancies on the CeO_2-NPS support are a contributing factor affecting the catalytic activity in CB oxidation. In addition, the higher ratio of O_{ads} and stronger interaction between the Mn and the ceria support may be two additional factors to improve the catalytic performance. In conclusion, the performance of CeO_2-NPS might benefit from a stronger interaction between Mn and the ceria support, higher concentrations of oxygen vacancies, and surface-adsorbed oxygen.

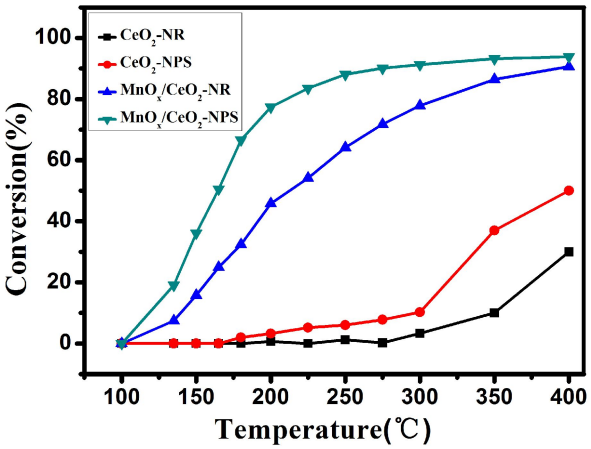

Fig. 8 MnO_x/CeO_2 catalysts for CB combustion, gas composition: 2500 mg/m^3 CB, 20% O_2, N_2 balance; GHSV = 20,000 h^{-1}.

Extended time stability tests of MnO_x/CeO_2 nanostructures with different support morphologies are shown in Fig. 9. Both catalysts show good stability after 30 h at 300 °C. Therefore, the two catalysts show good resistance to chlorine poisoning from CB.

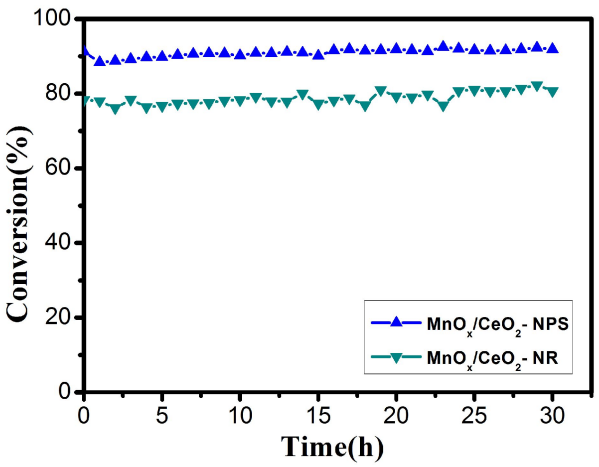

Fig. 9 The stability tests over the MnO_x/CeO_2 nanostructures for CB combustion at 300°C; gas composition: 2500 mg/m^3 CB, 20% O_2, N_2 balance; GHSV = 20,000 h^{-1}.

4. Conclusion

Manganese catalysts loaded on a ceria support with two different morphologies, MnO_x/CeO_2 nanoparticles (NPS) and MnO_x/CeO_2 nanorods (NR), were examined for their performance on the catalytic oxidation of CB. The morphology of the ceria support was observed to have a strong effect on the catalytic oxidation of CB. The MnO_x/CeO_2-NPS catalyst presented better catalytic activity compared to the MnO_x/CeO_2-NR catalyst. HRTEM and XRD analysis indicated that the CeO_2-NPS support preferentially exposed the (100) plane and are more likely to form anion vacancies and defects. The XPS and Raman results displayed a morphology dependence on the concentration of Mn^{4+} species, surface-adsorbed oxygen, and oxygen vacancies. Higher catalytic activity of MnO_x/CeO_2-NPS may be attributed to abundant Mn^{4+} species, oxygen vacancies and surface-adsorbed oxygen, which are associated with exposed (100) crystal planes. Furthermore, the extended time stability tests showed that both catalysts demonstrate resistance to chlorine poisoning. Thus, MnO_x/CeO_2-NPS catalysts can be considered as a potential material for the abatement of CVOCs.

Acknowledgments

We gratefully acknowledge the funding from the National Natural Science Foundation of China (No. 20873097, 21071113, 21471120), Natural Science Foundation of Hubei Province (No. 2011CDA049), International Cooperation Foundation of Hubei Province (2012IHA00201), Educatonal Commuission of Hubei Province of China (T201306).

Notes and references

Key Laboratory for Green Chemical Process of Ministry of Education, School of Chemistry and Environmental Engineering, Wuhan Institute of Technology, Xiongchu Avenue 693, Wuhan 430074, China.
E-mail: liushantang@mail.wit.edu.cn ; Fax:+86 27 87195001 ;
Tel: +86 27 87195001

1 X. Y. Wang, Q. Kang and D. Li, *Appl. Catal. B.,* 2009, **86**, 166-175.
2 H. Kominami, T. Nishi, K.Fuku and K. Hashimoto, *RSC Adv.,* 2013, **3**, 6058-6064.
3 J. J. Li, L. Li, W. Cheng, F. Wu, X.F. Lu and Z.P. Li, *Chem. Eng. J.*, 2014, **244**, 59-67.
4 Y. Z. Li, Z. Y. Fan, J. W. Shi, Z. Y. Liu and W.F. Shangguan, *Chem. Eng. J.*, 2014, **241**, 251-258.
5 J. W. Li, P. Zhao and S. T. Liu, *Appl. Catal. A.,* 2014, **482**, 363-369.
6 W. Tian, H. S. Yang, X. Y. Fan and X. B. Zhang, *Catal. Commun.*, 2010, **11**, 1185-1188.
7 J. W. Li, C. Song and S. T. Liu, *Acta Chim. Sinica.,* 2012, **70**, 2347-2352.
8 A. Jha, T. Chandole, R. Pandya, H. S. Roh and C. V. Rode, *RSC Adv.,* 2014, **4**, 19450-19455.
9 Z. Q. Zou, M. Meng and Y.Q. Zha, *J. Phys. Chem. C.,* 2010, **114**, 468-477.
10 M. A. Wolfovich, M. V. Landau, A. Brenner and M. Herskowitz, *J. Catal.*, 2007, **247**, 201-213.
11 Y. Liu, M. F. Luo, Z. B. Wei, Q. Xin, P. L. Ying and C. Li, *Appl. Catal. B.,* 2001, **29**, 61-67.
12 Y. F. Han, Z. Y. Zhong, K. Ramesh, F. X. Chen and L.W. Chen, *J. Phys. Chem. C.*, 2007, **111**, 3163-3170.
13 P. Gawade, B. Mirkelamoglu and U. S. Ozkan, *J. Phys. Chem. C.*, 2010, **114**, 18173-18181.

14 M. M. Schubert, S. Hackenberg, A. C. van Veen, M. Muhler, V. Plzak and R.J. Behm, *J. Catal*., 2005, **197**, 113-122.
15 H. Zhang, F. N. Gu, Q. Liu, G. G. Gao, L. H. Jia, T. Y. Zhu, Y. F. Chen, Z. Y. Zhong and F. B. Su, *RSC Adv.,* 2014, **4**, 14879-14889.
16 I. Soykal, B. Bayrama, H. Sohna, P. Gawadea, J. T. Millerb and U. S. Ozkana, *Appl. Catal A* ., 2012, **449**, 47-58.
17 M. Li, Y. H. Hu, C. C. Liu, J. G. Huang, Z. G. Liu, M. T. Wang and Z. H. An, *RSC Adv.,* 2014, **4**, 992-995.
18 X. S. Huang, H. Sun, L. C. Wang, Y. M. Liu, K. N. Fan and Y. Cao, *Appl. Catal. B*., 2009, **90**, 224-232.
19 Y. Liu, M. F. Luo, Z. B. Wei, Q. Xin, P. L. Ying and C. Li, *Appl. Catal. B*., 2001, **29**, 61-67.
20 H. X. Mai, L. D. Sun, Y. W. Zhang, R. Si, W. Feng, H. P. Zhang, H .C. Liu and C.H. Yan , *J. Phys. Chem. B*., 2005, **109**, 24380.
21 K. Zhou, X. Wang, X. M. Sun, Q. Peng and Y.D. Li, J. Catal., 2005, **229**, 206-212.
22 L. Ran, Z. Qin, Z. Y. Wang, X. Y. Wang and Q. G. Dai, *Catal. Commun*., 2013, **37**, 5-8.
23 R. S and M. Flytzani-Stephanopoulos, *Angew. Chem. Int. Ed*., 2008, **47**, 2884-2887.
24 H. J. Li, G. S. Qi, Tana, X. J. Zhang, W. Li and W. J. Shen, *Catal. Sci. Technol*., 2011, **1**, 1678.
25 S. N. Li, H. Q. Zhu, Z. F. Qin, G. F. Wang, Y. G. Zhang, Z. W. Wu, Z. K. Li, G. Chen, W. W. Dong, Z. H. Wu, L. R. Zheng, J. Zhang, T. D. Hu and Y. G. Zhang, *Appl. Catal. B*., 2014, **144**, 498-506.
26 Y. N. Liao, M. L. Fu, L. M. Chen, J. L. Wu, B. C. Huang and D. Q. Ye, *Catal. Today*., 2013, **216**, 220-228.
27 C. Song, Q. R. Yi, J. W. Li and S. T. Liu, *J. Funct. Mater*., 2014, **45**, 13050-13055.
28 R. H. Gao, D. S. Zhang, P. Maitarad, L. Y. Shi, T. Rungrotmongkol, H. R. Li, J. P. Zhang and W. G. Cao, *J. Phys. Chem. C*., 2013, **117**, 10502-10511.
29 Q. L. Zhang, C. T. Qiu, H. D. Xu, T. Lin, Z. E. Lin, M. C. Gong and Y. Q. Chen, *Catal. Today*., 2011, **175**, 171-176.
30 X. Y. Wang, Q. Kang and D. Li, *Appl. Catal. B*., 2009, **86**, 166-175.
31 A. Gupta, U. V. Waghmare and M. S. Hegde, *Chem. Mater*., 2010, **22**, 5184-5198.
32 Q. G. Dai, H. Huang, Y. Zhu, W. Deng, S. X. Bai, X. Y. Wang and G. Z. Lu, *Appl. Catal. B*., 2012, **117**, 360-368.
33 J. R. McBride, K. C. Hass, B. D. Poindexter and W. H. Weber, *J. Appl. Phys*.,1994, **76**, 2435-2462.
34 J. L. Zuo, Z. H. Chen, F. R. Wang, Y. H. Yu, L .F. Wang, X. H. Li, *Eng. Chem. Res*., 2014, **53**, 2647-2655.
35 X. W. Liu, K. B. Zhou, L. Wang, B. Y. Wang, Y. D. Li, *Jacks*., 2009, **131**, 3140-3141.
36 Y. Dai, X. Y. Wang, D. Li and Q. G. Dai, J. *Hazard. Mater*., 2011, **188**, 132-139.
37 H. Z. Chang, J. H. Li, J. Yuan, L. Chen, Y. Dai, H. Arandiyan, J. Y. Xu and J. M. Hao, *Catal. Today*., 2013, **201**, 139-144.
38 P. G. Harrison, I. K. Ball, W. Azelee, W. Daniell and D. Goldfarb, *Chem. Mater*., 2000, **12**, 3715-3725.

